Journal of
Materials Chemistry A

REVIEW

View Article Online
View Journal | View Issue

Cite this: *J. Mater. Chem. A*, 2019, **7**, 22148

Review of high entropy ceramics: design, synthesis, structure and properties

Rui-Zhi Zhang *[a,b] and Michael J. Reece *[a]

High entropy ceramics are novel materials with no less than four different cations or anions. The development of high entropy ceramics follows the 'configurational entropy stabilized single phase' concept, which was first demonstrated for high entropy metal alloys in 2004. The advantages of high entropy ceramics are their compositional and structural diversity, and many of them have a band gap, which makes them potential functional materials for a wide range of applications. They have recently generated significant interest with the publication of 70+ related papers since 2015. In this review we have summarized the recent progress in this rapidly growing field. We emphasize the progress by researchers to answer the following three fundamental questions for high entropy ceramics: (1) which combinations of cations or anions can be synthesized as single-phase materials; (2) are the component elements truly random down to the atomic scale; and (3) what new physics, properties and applications will the incorporation of multi-elements elements bring. These fundamental questions are still open at this stage and warrant further studies. The objective of this review is to give a comprehensive overview of the literature to date on high entropy ceramics and to guide further investigation in this emerging field.

Received 28th May 2019
Accepted 23rd July 2019

DOI: 10.1039/c9ta05698j

rsc.li/materials-a

1. Introduction

High entropy ceramics (HECs), sometimes also referred to as high entropy compounds, are single phase ceramics with no less than four types of cations or anions. The concept of high entropy ceramics is inherited from the field of high entropy alloys (HEAs). The two families of materials are fundamentally different, and hence their applications are also different. Since

Rui-Zhi Zhang received a Ph.D. in condensed matter physics in 2010 from Shandong University in China. After completing Ph.D. he worked in Northwest University in Xi'an, China as an associate professor. In 2014, he held the position of Marie Curie Research Fellow under the guidance of Prof Michael J. Reece at Queen Mary University of London. His research interests include data-driven ceramics design utilizing density functional theory and deep neural networks, and spark plasma sintering of thermoelectric ceramics and high entropy ceramics.

Michael J. Reece's research group is currently focused on the development of field (electric, magnetic and gravity) assisted processing to produce nanostructured, textured, hierarchical and non-equilibrium functional ceramics, including thermoelectrics and high entropy ceramics. This includes the recently established MagMat facility for the synthesis and processing of materials in strong magnetic fields (15T). A longterm objective of his work is to commercialise materials prepared by field assisted processing through knowledge transfer and spin-outs. He is a Director of Nanoforce Technology Ltd, a spin-out company of QMUL. Nanoforce focuses on the development of new, scalable processing routes for nanomaterials that can be commercialised.

---

[a] *School of Engineering and Materials Science, Queen Mary University of London, London E1 4NS, UK. E-mail: m.j.reece@qmul.ac.uk*

[b] *School of Physics, Northwest University, Xi'an 710069, China. E-mail: zhangrz@nwu.edu.cn*

the invention of HEAs in 2004,[1,2] intensive research on HEAs in the past decade has led to many interesting results, such as enhanced hardness and strength.[3,4] Due to the intensive research on HEAs, HECs have now become a new focus in the search for novel materials. Similar to HEAs, HECs consist of multi-component elements in a single phase, for which their large configurational entropy contributes to their formation.[5] In contrast to metallic HEAs, HECs are typically semiconductors or insulators with a band gap, which makes them potentially useful functional materials. For example, high entropy chalcogenides can be good thermoelectric materials due to their large Seebeck coefficient and low thermal conductivity.[6,7] Recently, it was reported that charge-induced disorder in high entropy oxides controls thermal conductivity;[8] this opens up new possibilities to improve the performance of thermoelectric materials.

Another advantage of HECs is that they have ample structural diversity (see Fig. 1). The members of the HEC family are increasing rapidly. The earliest reported work on HECs was on coating materials, typically nitrides[9–11] and carbides.[9] In 2015 Rost *et al.* reported on entropy-stabilized HEC oxides.[5] This work stimulated interest in the properties of these materials, such as dielectric,[12] Li-battery[13] and low thermal conductivity.[8] In the following three years, researchers extend the family members to include diborides,[14] chalcogenides,[7] silicides[15] and intermetallics such as half Heusler,[16] for a broad range of applications from structural to functional. The growing number of members studied is bringing structural diversity. The earlier reported HECs all had rock salt structure, including nitrides, carbides and the well-studied $Mg_{0.2}Co_{0.2}Ni_{0.2}Cu_{0.2}Zn_{0.2}O$. To date there are eight structural types, with more likely to be reported in the near future (Fig. 1). To name a few, cubic perovskite oxides,[17] fluorite oxides[18] and hexagonal diborides.[14]

The review consists of four sections covering design of single phase HECs, typical synthesis methods, atomic scale structure characterization, properties and applications. The structural and element diversity of HECs makes the design and prediction of single phase materials very important, and this topic will be discussed in detail in the following section.

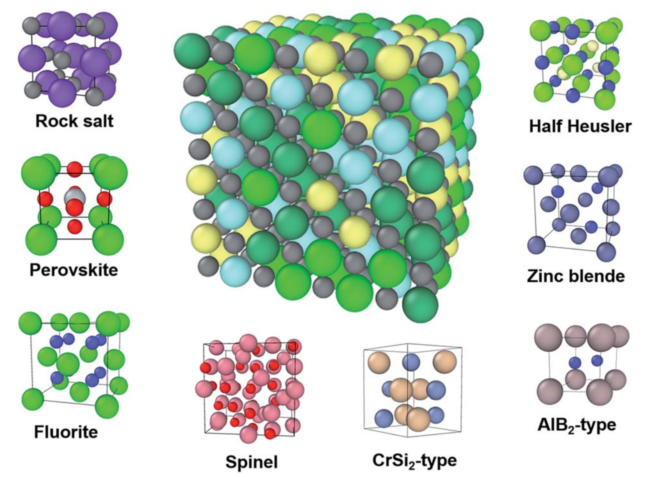

Fig. 1 Structural diversity of the HEC family. The central image shows a supercell of a HEC rock salt structure; anions are dark grey spheres and cations are randomly distributed. The unit cells are based on HECs that have been successfully fabricated.

2. Design of single phase HECs

Developing new materials is always one of the fundamental driving forces in materials science. Therefore, predicting yet-unknown single solid solution phases is of great interest to the high entropy materials community. For such prediction, a model, either based on descriptors or on the calculation of Gibbs free energy, is needed. Then this model can be used to predict the stability of a given formula in a given crystal structure, or to explore the combinatorial space to identify stable compositions. Unlike for the HEA community, the design of HECs is at a very early stage. Currently, in most HEC papers the authors simply chose a group of elements in a specific part of the periodic table. Only a few papers deal with the design of materials, of which most use a descriptor approach.

2.1 Using descriptors

An underlying assumption is that stable single-phase solid solutions have something in common that can be described by descriptors. The descriptor-based approach can be tracked to the pioneering work of William Hume-Rothery,[19] in which several rules, later coined as the 'Hume-Rothery rules', describe the conditions under which solid solution alloys can be formed. It is worth noting that some descriptors used in the design of HECs can be considered as derivatives of these rules.

2.1.1 Examples of descriptors. Liu *et al.*[6] proposed a descriptor for judging atomic solubility in a two-component solid solution compound when the crystal structures of the components are the same

$$\delta = \frac{\overline{R^*}(\Delta R^*)^2}{Z}\bar{G} \qquad (1)$$

where $\overline{R^*}$ is the average effective lattice constant and $\Delta R^*$is the difference in effective lattice constant, Z is the number of formula units per unit cell, and $\bar{G}$ is the average shear modulus. A small δ value means a low internal strain energy and high atomic solubility, and *vice versa*. For multi-component solid solutions, the average $\bar{\delta}$ value can be calculated by averaging the values for all of the quasi-binary solid solutions. Using a phenomenological formula for the enthalpy of mixing and configurational entropy, the upper bound of $\bar{\delta}$ values were calculated as 2.08, 2.92, 3.58, and 4.12 GPa $Å^{-3}$ for binary, ternary, quaternary and 5 component solid solution compounds, respectively (Fig. 2). These criteria were tested by experimentally fabricating several multi-component materials, *e.g.* $(Cu/Ag)(In/Ga)Te_2$-, $Cu_2(S/Se/Te)$-, and (Pb/Sn/Ge/Mn)Te. X-ray diffraction analysis showed that all these materials are phase pure without any obvious impurity phases (Fig. 2).

Using a data-driven approach, Zhang *et al.*[7] identified all of the diamond-like Cu/S containing compounds in the Inorganic Crystal Structure Database (ICSD), and then all of the cation–sulfur bond lengths in the 49 identified compounds were

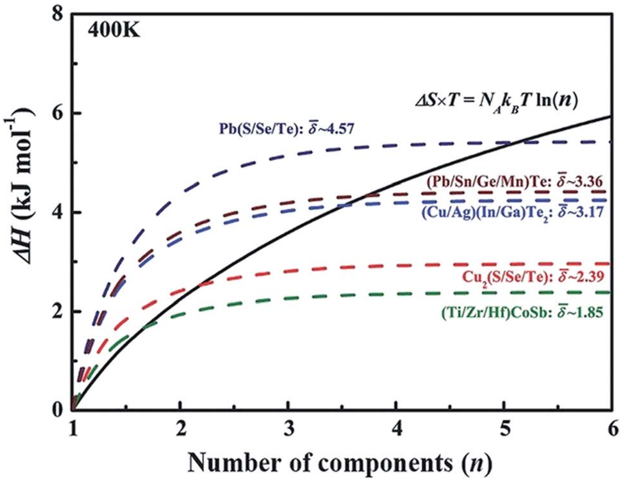

Fig. 2 The dashed lines illustrate internal strain energy as a function of the number of components for several solid solution compounds. The black solid line represents the energy contributed by configurational entropy. Reproduced with permission. Copyright 2017, John Wiley and Sons.[6]

calculated using the ICSD crystallographic information files (CIFs). These bond length values were compared with those calculated from the bond valence model (Fig. 3), and it was found that, although there was general agreement, the bond length of some cations, such as Cu, Ge and Sn, have a large variation and they can be considered as 'soft atoms'. These atoms were then used in the design of high entropy sulphides to reduce the local strain energy. By considering the Hume-Rothery rules, two high entropy sulphides, metallic $Cu_5SnMgGeZnS_9$ and semiconducting $Cu_3SnMgInZnS_7$, were designed and then successfully fabricated as single-phase dense ceramics with homogenously distributed cations.

Jiang *et al.* fabricated several high-entropy perovskite oxides,[17] and concluded that the Goldschmidt's tolerance factor, instead of cation-size differences on a specific lattice site, influences the formation and temperature-stability of single cubic perovskite solid solutions. They found that the calculated tolerance factors for all six compositions that form single phase high-entropy perovskite phases were close to unity ($0.97 \leq t \leq 1.03$). They suggested that a Goldschmidt tolerance factor close to unity ($t \approx 1.00$) is important, but not a solely sufficient criterion to form a single high-entropy perovskite phase.

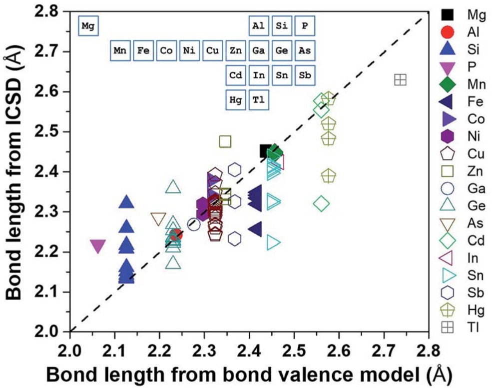

Fig. 3 Bond length calculated using ICSD CIFs and BVM. The inset shows the position of the elements in the periodic table. Reproduced under the terms of the CC-BY 4.0 license. Copyright 2018, the authors, published by ACS Publications.[7]

The above models illustrate the use of descriptors related to mixing enthalpy. There has also been an attempt to develop an 'entropy descriptor'. K. Vecchio *et al.* proposed 'entropy forming ability (EFA)' as a descriptor to address the synthesizability of HECs from first principles.[20] The EFA was estimated as the inverse of the standard deviation of the energy distribution spectrum of the enthalpies of all of the possible atom configurations of 10-atom supercells

$$\mathrm{EFA} = \left(\sqrt{ \frac{\sum_{i=1}^{n} g_i (H_i - H_{\mathrm{mix}})^2}{\left(\sum_{i=1}^{n} g_i \right) - 1} } \right)^{-1} \tag{2}$$

where n is the total number of sampled geometrical configurations, and g_i are their degeneracies. H_i is the enthalpy of formation at zero temperature of a supercell, and H_{mix} is the average of the enthalpies H_i of all of the possible supercell configurations. A larger EFA value corresponds to a larger entropy for a given composition.

The EFA descriptor was used to screen all of the possible compositions of five-metal carbides selecting from 8 chosen cations (Ti, Zr, Hf, V, Nb, Ta, Mo, W). Then the six compositions with the highest EFA values (the highest one is $MoNbTaVWC_5$ with EFA = 125 atom eV^{-1}) were experimentally fabricated as single phase HECs, and three compositions with low EFA values (the lowest one is $HfMoVWZrC_5$ with EFA = 37 atom eV^{-1}) were found to be multi-phase. These experimental results demonstrate the effectiveness of the EFA descriptor.

2.1.2 Discussions of descriptors.

The choice of descriptor determines the accuracy of the prediction. Therefore, more suitable and reliable descriptors are needed. There are many possible choices for descriptors. Ramprasad *et al.*[21] categorized descriptors based on gross-level properties, molecular fragment-level, and sub-Angstrom-level. For example, EFA is a gross-level descriptor and atomic size is a molecular fragment-level descriptor. Considering the existing dozens of descriptors in the literature and the millions of their combinations as potential descriptors, the development of a HEC stability descriptors is only at its very early stage. Choosing the best descriptor relies on either physical/chemical domain knowledge, or data-driven statistics.[22] It is worth noting that sometimes there are different definitions for a given descriptor. Take atomic size as an example, the ionic radius can be Shannon's radius,[23] or bond valence model based,[24] or density functional theory calculation based[25] This presents large diversity and special attention should be paid to the choice of descriptor.

A major criticism of descriptor based chemical models comes from the point view of physics. Researchers argue that phase stability is not an intrinsic property of a material, and hence kinetics and all of the competitive phases must be considered to predict stability.[26] However, the descriptors are implicitly related to Gibbs free energy, and that is the reason why some descriptors are also referred as 'empirical thermophysical parameters'.[27] For example, similar atomic radius usually means low strain energy, which reduces the enthalpy of mixing. Although Gibbs free energy based physical models are widely accepted as more quantitatively accurate, the use of descriptors has some merits such as they are easy to use, and can be quite effective under certain circumstances.

2.2 Using Gibbs free energy

Gibbs free energy calculations and phase diagrams can give quantitative information on phase stability. The Gibbs free energy can be calculated using density functional theory (DFT) or other empirical methods, such as the Calculate Phase Diagrams (CALPHAD) method that is used to calculate phase diagrams. A modern trend is to combine empirical methods and DFT. To date, there are few works on the calculation of Gibbs free energy for the prediction of the stability of HECs. Therefore, this section will mainly focus on the principles and briefly introduce their application to HEAs. For comprehensive reviews on these method's as applied to HEAs, see the in-depth reviews by M. C. Gao *et al.*[27] and M. Widom.[28]

2.2.1 Definition of Gibbs free energy. At constant temperature and pressure, the Gibbs free energy of a solid has a minimum value in a state of thermal equilibrium. The Gibbs free energy is a thermodynamic potential in thermodynamics

$$G = H - TS \tag{3}$$

where H, T and S are enthalpy, temperature and entropy, respectively. A larger entropy favours a lower Gibbs free energy and hence phase stability. In general, under the assumption that each microstate has equal probability, the entropy of a system relates to its number of microstates Ω

$$S = k_{\mathrm{B}} \sum \ln \Omega \tag{4}$$

For an alloy system, the entropy is contributed to by vibrational entropy, configurational entropy and other terms. For a completely disordered alloy, and using Sterling's approximation, the configurational entropy, sometimes referred to as entropy of mixing, is

$$S_{\mathrm{conf}} = -R \sum_{i=1}^{n} c_i \ln c_i \tag{5}$$

where R, n and c_i are the ideal gas constant, the number of components, and the atomic fraction of component i, respectively. More components, *i.e.* larger n, results in higher S_{conf}. For a given number of components, S_{conf} has the maximum value when all the components have the same atomic fraction, *i.e.* equimolar. The importance of entropy for single phase stabilization was demonstrated in the "entropy-stabilized oxide" $Mg_{0.2}Co_{0.2}Ni_{0.2}Cu_{0.2}Zn_{0.2}O$,[5] as evidenced by the temperature dependence of its stability, with a reversible solid-state transformation between a multiphase and single-phase (high temperature) state. A recent survey of high entropy oxides listed all 10 of the known high entropy oxides, of which only three are entropy stabilized.[29] Therefore, the design of HECs should consider both minimizing enthalpy as well as maximizing entropy.

2.2.2 DFT models. Due to the intrinsic disordered nature of HECs, the construction of a DFT model is not straightforward. The reason is that the periodic condition applied to finite size models introduces some order. Due to limited computational power, DFT models are usually small, introducing unrealistic order compared with the complete disorder in an infinite system. To maximize the randomness in a limited size supercell, Zunger *et al.* proposed special quasi-random structures (SQS) in 1990.[30] Using statistical techniques based on a lattice model, SQS can be determined as the best possible special periodic structure, with a small number of atoms per unit cell, in which the correlation functions in the first few nearest neighbours can be captured as those in a random solid solution. This way the error introduced by the periodic conditions of the cell is mainly between more distant neighbours. SQS is effective when the interactions between distant neighbours are nearly negligible. Farid Akhtar *et al.*[31] used the Alloy Theoretic Automated Toolkit (ATAT)[32] code to construct the SQS of B_4-$(HfMo_2TaTi)C$, and calculated the enthalpy of formation as −2.29 eV per unit cell. Ye *et al.* calculated the enthalpy of formation of SQS $(Zr_{0.25}Nb_{0.25}Ti_{0.25}V_{0.25})C$ as 5.526 kJ mol^{-1}.[33] They both used the calculation results to guide the synthesis of HECs, and obtained experimentally single phase ceramics.

An alternative approach is the coherent potential approximation (CPA),[34] which approximates a configurationally random alloy with an effective medium that is determined self-consistently from the condition of stationary scattering. This approach only considers compositional disorder, and local lattice distortions are totally ignored. Compared to the SQS approach, in which a large cell is used and local distortion is included, the computational cost for CPA is relatively low, as only a unit cell with pseudo-mixed-atoms is used. Although CPA is less accurate, it is still useful and effective when local distortions are not important to the properties of interest. Another advantage of CPA is that the composition can be varied continuously.

2.2.3 Methods other than DFT. CALPHAD uses databases containing a large amount of thermodynamic data, which is obtained from experiments or DFT calculations.[35] Based on the databases, numerical interpolation or extrapolation schemes are used to calculate the phase diagram and to predict new stable compositions. CALPHAD excels at modelling phase diagram topology with high reliability. The reliability of CALPHAD rests on the available database and accurate expression of the Gibbs free energy. For instance, to predict the phase stability of a new ternary phase, all of the thermodynamic data of the related binary phases is needed. For the same reason, CALPHAD is more accurate in the regions near the edges of the phase diagram, *i.e.* when the material has one element as the main component and the amount of other elements is relatively small. For HECs in the central region of the phase diagram, where the components are nearly equimolar, the absence of the necessary compounds in the databases will make the prediction less reliable.[36]

Cluster expansion[37] refers to the mathematical expression of a physical quantity in the form of a series expansion. The main terms of the series represent a corresponding noninteracting system, and the subsequent terms describe the interactions between the particles. This method is physically strict and systematic in principle, although its application to real systems is quite complicated. It has been applied to alloys for a long time.[38,39] The implementation of cluster expansion for alloy systems can be found in programs such as universal cluster expansion (UNCLE)[40] and alloy theoretic automated toolkit (ATAT),[32] in which the free energies of HEC phases can be calculated and hence the phase diagram predicted. Cluster expansion has been used together with DFT calculations for high-throughput screening for novel high entropy materials.[41]

3. Synthesis and processing of HECs

So far, three methods have been used to synthesise HECs, namely solid-state reaction, wet chemical, and epitaxial growth. In this section the discussion mainly focuses on solid state reaction, in which the kinetics of formation for different HECs has been investigated. The other two methods have so far only been applied to oxides, and are briefly covered at the end of this section.

Solid-state reaction is the predominant synthesis route used to prepare HECs, in which the powders are usually produced by mechanochemistry or mixing of the precursor powders during ball milling, and then the resultant powders are sintered. HECs prepared from low melting point precursors, such as chalcogenides, are synthesised by mechanochemistry during ball milling. In this scenario, inter-diffusion of the components begins during ball milling, and the XRD diffraction peaks of precursors disappear in the ball milled powders.[7] For HECs from high melting point precursor, such as oxides and carbides, ball milling is used only to mix the powder, and the HECs are synthesised during sintering, *i.e.* the inter-diffusion processes of the components mainly occur during sintering.

E. Castle *et al.*[42] found that using same processing conditions, ZrC appeared as a second phase in HEC (Hf–Ta–Zr–Ti)C, while (Hf–Ta–Zr–Nb)C was single phase. They attributed this observation to the slower diffusion of ZrC in the HfC–TaC–ZrC–TiC mixed phases than in HfC–TaC–ZrC–NbC. To explain the different diffusion rates of ZrC, they suggested the following order of inter-diffusing rates: TaC $<$ ZrC $\sim$ HfC $<$ NbC $<$ TiC, based on the vacancy formation energies, known melting points (relative atomic mobility), metal atomic radius and lattice parameters of the individual carbides. Therefore, TiC–TaC or NbC–TaC inter-diffusion occurs first in the mixed phases HfC–TaC–ZrC–TiC and HfC–TaC–ZrC–NbC, respectively, as TiC or NbC are the fastest and TaC is the slowest diffusing components. Incorporating TiC reduces the lattice parameter of TaC, making it more difficult for the larger ZrC to inter-diffuse into the mixed carbide phase, thus slowing down the kinetics of the ZrC inter-diffusion. By contrast, incorporating NbC increases the lattice parameter of TaC and hence makes the diffusion of ZrC easier.

W. Hong *et al.*[43] did a similar analysis for (Mg,Co,Ni,Cu,Zn)O. From the XRD spectra of the HECs heat treated at temperatures from 650 to 825 °C, they found that the inter-diffusion between the components started at 650 °C; the diffraction peaks of MgO and CoO started to merge, and the peak intensity of the other components became weaker. With increasing temperature, the characteristic peaks of NiO, ZnO and CuO disappeared successively. This observation indicates that CoO and MgO have the fastest inter-diffusion rates while ZnO and CuO have the slowest. They also found that the rate at which species can be incorporated into the HEC structure may relate to metal vacancy formation energies, while no correlation was found between the cation radii and the observed interdiffusion behaviour.

Another kinetic effect relates to meta-stability. Some HECs can be synthesised at high temperatures but are meta-stable at room temperature, therefore phase separation tends to occur during the cooling down period after sintering. A common processing routine to deal with this is quick quenching, *i.e.* samples were quenched from around 1000 °C to room temperature in less than one minute.[5] This technique has been applied to various types of compounds, such as oxides[5] and half Heuslers.[16]

The wet chemical methods used for synthesising HECs include nebulised spray pyrolysis, flame spray pyrolysis and reverse co-precipitation. They have been used to prepare nanoscale oxide powders of (Mg,Co,Ni,Cu,Zn)O,[44–46] PtNiMgCuZnCoO$_x$,[47], (Li$_x$(Co$_{0.2}$Cu$_{0.2}$Mg$_{0.2}$Ni$_{0.2}$Zn$_{0.2}$)OF$_x$)[48] and HEC oxides.[44,49] High entropy metal oxide nanotube arrays were also prepared by anodic oxidation of TaNbHfZrTi HEA precursors.[50]

The third HEC synthesis routine is epitaxial growth of films. So far in the literature only pulsed laser deposition (PLD) has been used to prepare HEC oxides. One advantage of this method is that single crystals can be grown,[51] therefore grain boundary segregation is avoided and precise elemental ratios can be achieved. Epitaxial growth is also useful for preparing structures that are not possible to produce by solid state reaction and wet chemical methods, such as superlattices and heterostructures.[52]

4. Atomic scale structure

From the point view of crystal structure configuration, the major difference between HEAs and HECs is that the latter usually have a uniform anion/cation sub-lattice, and only have disorder on the other sites. The sub-lattice, on one hand, reduces the possible configurational entropy; while on the other hand, it reduces short range order (SRO), which increases the configurational entropy of the cations.[5]

SRO means order over distances comparable to interatomic distances. Taking a two-component alloy with components A and B as an example: the interaction energies E_{A-A}, E_{B-B} and E_{A-B} are usually different, so some atomic pair configurations are more energetically favourable than others, and hence the number of lower energy configurations is much greater than in the completely random case. This results in SRO, which reduces the configurational entropy compared to the completely random configuration. In HECs, a uniform anion sub-lattice can reduce SRO. In a recent paper, Rost *et al.* proposed that the cations in high entropy oxides are perhaps more disordered than in a HEA.[5] As shown in Fig. 4, the cations in the oxide have the same coordination environment: all have six nearest-neighbour octahedral coordination with oxygen ions. As the interaction energy is mainly contributed to by the nearest-neighbour, the configurational energy difference on different cation sites becomes small, and hence the preference of cations pairs and SRO is less likely. This increases configurational entropy and favours single phase formation.

4.1 General structure features

The structure of HECs involves different length scales. An ideal HEC should have a lattice with long-range periodicity but compositional disorder, *i.e.* the periodic lattice sites are randomly occupied by the constituent atoms. Therefore, the structural characterization of HECs is mainly concerned with the determination of single phase (*i.e.* long-range periodic lattice) and the homogeneity of the constituent elements (*i.e.* truly random occupation). It is worth noting that although in most HEC development the achievement of a homogeneous single phase is emphasized, sometimes second phases and/or phase separation can be beneficial to the properties. For example, ferroelectric relaxors contain nano polar regions, which confer high dielectric energy storage and giant piezoelectric properties,[53] and thermoelectric composites with nanoscale phase separation confers low lattice thermal conductivity.[54] While such effects could be useful, this topic has not yet been covered by the HEC community. In the following we only focus on the techniques for charactering single phase, local atom structure and chemical homogeneity.

Long-range periodicity is usually tractable through analysis of Bragg peak intensities in XRD. For the compositional distribution, SEM-EDS can be used to find if the elements are homogeneously distributed at the microscale. XRD and SEM-EDS are commonly used techniques to characterise HECs and will not be discussed in detail. In this review we focus on less common techniques dealing with nanoscale atom distribution and the local lattice structure of HECs. The local lattice distortion is an important structural feature of HECs that needs to be characterised. It is worth noting that severe lattice distortion is one of the four fundamental concepts proposed for HEAs.[55,56]

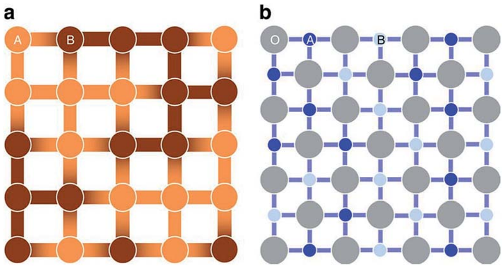

Fig. 4 A schematic representation for the comparison of (a) a random binary alloy and (b) a random pseudo-binary oxide. The darkness of the atoms illustrates differences in electronegativity, and the darker bonds more localized negative charge. In the oxide, the nearest neighbour cations are separated by uniform anion sub-lattice. Reproduced under the terms of the CC-BY 4.0 license. Copyright 2015, the authors, published by Springer Nature.[5]

4.2 Atomic scale structural features

4.2.1 Element distribution. To determine element distribution at the nanoscale, there are currently two techniques that can be used, scanning transmission electron microscopy (STEM) and Atomic Probe Tomography (APT). Rost *et al.* used STEM EDS to analyse the structure and chemistry on the local scale of $Mg_{0.2}Co_{0.2}Ni_{0.2}Cu_{0.2}Zn_{0.2}O$ thin films on a (100) MgO substrate prepared using pulsed laser deposition.[5] They found a homogeneous distribution of the cations in the high-angle annular dark-field signal (HAADF) images. Sarkar *et al.* also found nanoscale homogeneous distribution in powder particles of the same composition.[46] Atomic scale homogeneous element distribution has also been reported for $Ba(Zr_{0.2}Sn_{0.2}Ti_{0.2}Hf_{0.2}Nb_{0.2})O_3$ thin films grown on $SrTiO_3(001)$,[51] and the following ceramics $(Hf_{0.2}Zr_{0.2}Ta_{0.2}Nb_{0.2}Ti_{0.2})C$,[57,58], $(Ti_{0.2}Hf_{0.2}V_{0.2}Nb_{0.2}Ta_{0.2})C$,[59], $(Zr_{0.25}Nb_{0.25}Ti_{0.25}V_{0.25})C$,[33], (Hf–Ta–Zr–Nb)C,[60] and equal-molar $TiN_{0.3}$/VC/NbC/TiC/TaC/Mo_2C/WCs,[61] based on STEM-EDS and HAADF images.

Another useful technique for investigating atom scale element distribution is APT. It is a destructive method that can be used for 3D chemical composition imaging at the atomic scale.[62] Liu *et al.* used APT to check the distribution of atoms at the atomic-scale in $Cu_2S_{1/3}Se_{1/3}Te_{1/3}$ ceramics (Fig. 5a).[6] Chellali *et al.* used APT to study the atomic scale cation distribution in three types of high entropy oxides, rock-salt $(Co_{0.2}Cu_{0.2}Mg_{0.2}Ni_{0.2}Zn_{0.2})O$, fluorite $(Ce_{0.2}La_{0.2}Pr_{0.2}Sm_{0.2}Y_{0.2})O_{2-\delta}$, and perovskite $(Gd_{0.2}La_{0.2}Nd_{0.2}Sm_{0.2}Y_{0.2})$ $(Co_{0.2}Cr_{0.2}Mn_{0.2}Fe_{0.2}Ni_{0.2})O_3$.[63] In the chalcogenides and oxides, APT results showed that all of the anions or cations were homogenously distributed at the atomic scale and no significant aggregation was found.

4.2.2 Local environment and distortion. Local structure includes chemical environment and local lattice distortion around the individual cations/anions. This problem falls within the domain of the extended X-ray absorption fine structure (EXAFS) and total scattering/pair distribution function (PDF) techniques, which have been applied to HECs to study their local structures.

Rost *et al.* quantified the local atomic structure of $Mg_{0.2}Co_{0.2}Ni_{0.2}Cu_{0.2}Zn_{0.2}O$ on an element-by-element basis (Fig. 5b).[5,64] They found that the metal–oxygen bond lengths varied for each cation, with notable distortion around the Cu–O polyhedral. The interatomic distances of second nearest neighbours (*i.e.* the metal–metal pairs) were found to be uniform. By combination of model fitting of experimental data and DFT calculations, they showed that distortion from an ideal rock salt structure occurs primarily through distortion of the oxygen sublattice, with the cations distributed randomly on their FCC sublattice. Using the same method, Harrington *et al.*

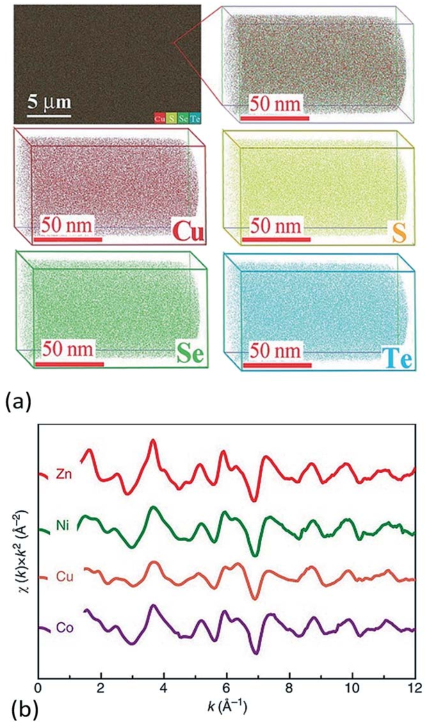

Fig. 5 (a) 3D-Atomic maps for $Cu_2S_{1/3}Se_{1/3}Te_{1/3}$ from Atomic Probe Tomography (APT) detection, which suggest that all elements are homogenously distributed at nanoscale.[6] (b) Extended X-ray absorption fine structure (EXAFS) measured for $Mg_{0.2}Co_{0.2}Ni_{0.2}Cu_{0.2}Zn_{0.2}O$. The oscillations for each element occur with similar relative intensity and at similar reciprocal spacing, which suggests a similar local structural and chemical environment for each.[5] (a) Reproduced with permission. Copyright 2017, John Wiley and Sons.[6] (b) Reproduced under the terms of the CC-BY 4.0 license. Copyright 2015, the authors, published by Springer Nature.[5]

found that each of the metals has a similar local surroundings in $(V_{0.2}Nb_{0.2}Ta_{0.2}Mo_{0.2}W_{0.2})C$.[59] It is worth noting that some elements are missing in these EXAFS experiments due to either the energetic limitations of the beamline (*e.g.* Mg in HEC oxides) or absorption edge overlap (*e.g.* W and Ta in the HEC carbides).

Total scattering describes the probability of finding atoms a certain distance away from another atom.[65] Peng *et al.* generated X-ray PDF spectra for equal-molar $TiN_{0.3}$/VC/NbC/TiC/TaC/Mo_2C/WC. By fitting the PDF profile using the PDF gui code with an ideal FCC structural model and a random atomic arrangement, they concluded that the HEC carbide was a well-defined single phase with negligible lattice distortion.[61]

The local distortion can also be indirectly detected by electron paramagnetic resonance (EPR), which exploits the physical properties of unpaired electrons in materials, *e.g.* electrons of transition metal ions. Berardan *et al.* probed the geometry of the Cu ion in $(MgCoNiCuZn)_{0.9}Li_{0.1}O$ and $(MgCoNiZn)_{0.74}Cu_{0.26}O$ lattices.[66] They found that the EPR signal of the first composition was isotropic, which corresponds to the octahedral environment expected from the rock salt structure. While the second composition, *i.e.* the Cu-rich one, had a distorted EPR signal, which indicates that there was significant distortion from the ideal rock salt structure. The deviation originates from a controllable Jahn–Teller distortion. DFT calculations from Rák *et al.* support the experimental results.[67]

4.2.3 Atomic simulation. Atomic scale simulation tools, such as DFT calculations and molecular dynamics, can also be used to investigate the local structure of HECs. In these simulations, it is possible to investigate the displacement of each individual atom or individual bond length, therefore it is very informative and can be complimentary to experimental characterisation techniques. As the structural details are stochastic, they are typically shown in a statistical way.

Anand *et al.* constructed 23 536 supercells for the 5-component (Mg,Co,Cu,Ni,Zn)O system with a rock salt lattice, and each supercell had 1000 cations and 1000 oxygen anions.[68] Molecular dynamics using the Buckingham interatomic potential was conducted to capture the local structures. It was found that in supercells with higher configurational energies, less Cu^{2+}–Cu^{2+} pairs but more Cu^{2+}–Zn^{2+} pairs were present. No particular ordering was found for the other 13 types of pairs

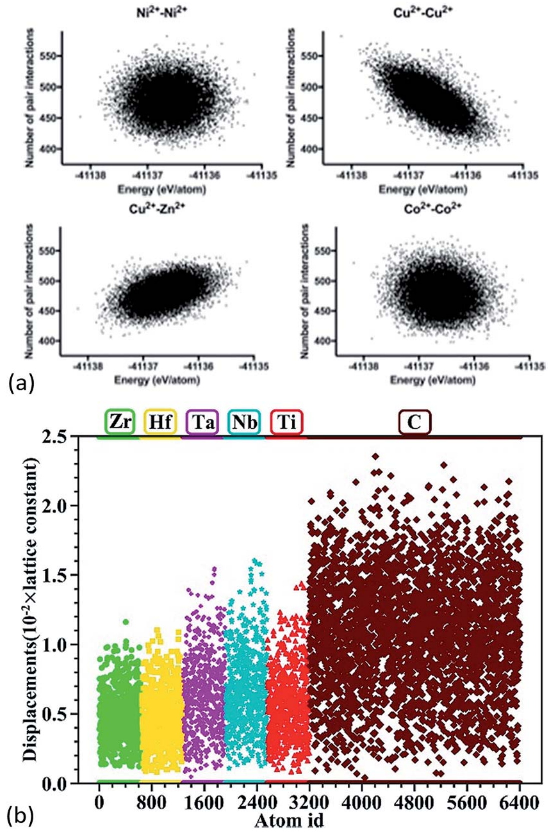

Fig. 6 (a) Molecular dynamics of 23 536 (Mg,Co,Cu,Ni,Zn)O supercells. The dots show the dependence of number of next nearest-neighbour cation–cation pairs on the total energies of formation of the supercells.[68] For the 15 possible types (of which only 4 are shown here) of cation–cation pairs, only Cu^{2+}–Cu^{2+} and Cu^{2+}–Zn^{2+} pairs show an energetical dependence. (b) DFT calculations of $(Hf_{0.2}Zr_{0.2}Ta_{0.2}Nb_{0.2}Ti_{0.2})C$. The dots show atomic displacements of each individual atom from its ideal position in a rock salt structure.[57] Reproduced with permission. (a) Copyright 2018, Elsevier.[68] (b) Copyright 2018, John Wiley and Sons.[57]

(Fig. 6a). Based on nearest-neighbour distance analysis, it was found that Cu^{2+}–Cu^{2+} and Cu^{2+}–O^{2-} pairs have lowest cation–cation and cation–anion bond lengths with minimum variation, respectively.

Ye *et al.* built 100 supercells for rock salt $(Hf_{0.2}Zr_{0.2}Ta_{0.2}Nb_{0.2}Ti_{0.2})C$.[57] Each supercell contained 64 atoms with a random distribution of the metal atoms, and the cation stoichiometry was nearly equimolar. These supercells were then fully relaxed using DFT calculations to give total energies and atomic positions. The displacement of the atoms shows that generally the anion (*i.e.* carbon) has larger displacements than the cations (Fig. 6b), suggesting that the lattice distortion in these HEC carbides occurs mainly through the anion sublattice. A similar anion lattice distortion was also reported for DFT calculations of the HEC oxide[64,69] $Mg_{0.2}Co_{0.2}Ni_{0.2}Cu_{0.2}Zn_{0.2}O$ and sulphide $Cu_5SnMgGeZnS_9$.[7]

5. Properties and applications

The review of properties of HECs in this section shows that the addition of multiple elements not only allows new materials to be synthesized but also leads to an enhancement of physical effects and potentially new physics in the case of thermal conductivity. It also raises some fundamental questions, such as, the meaning of band structure in the case of semiconductor materials and the origin of strengthening effects in plasticity. The types of HECs for specific applications are listed in Table 1.

Design models for property predictions are useful to guide HEC composition selection. As listed in Table 1, they are generally well developed and have gained great success in simple crystal structures. The main challenge for applying them to HECs lies in the domain of DFT and MD, *i.e.* the limited SQS size in DFT due to the demanding computational power, and the lack of availability of accurate interatomic potentials for multi-component systems in MD. The properties modelling of HECs is at its infant stage but is growing rapidly.

5.1 Thermal conductivity

The thermal conductivity of solids is determined by both phonon and electron transport. In the literature on HECs, the phonon part, *i.e.* the lattice thermal conductivity, has been the most commonly reported and analysed. The electronic contribution to the thermal conductivity has, however, barely been discussed. Therefore, this section mainly focuses on the lattice thermal conductivity.

5.1.1 Experimental results. Liu *et al.*[6] established a relationship between configurational entropy and lattice thermal conductivity by summarizing the results of several multicomponent compounds. They attributed the lattice thermal conductivity reduction to strong mass and strain fluctuations between the various components. Therefore, an increasing number of components results in both an increasing configurational entropy and a lower lattice thermal conductivity. To reach the minimum lattice thermal conductivity ($\kappa_{\min}$), the required number of components varies for different materials. At least 5 or 6 components are needed when the matrix compounds have high initial thermal conductivity, *e.g.* half Heusler; whereas only 3 or 4 components are required for compounds with a moderate initial lattice thermal conductivity, *e.g.* Bi_2Te_3.

J. Braun *et al.*[8] investigated the thermal conductivities of five-cation $MgCoNiCuZnO_5$ and six-cation $MgCoNiCuZnXO_6$ (X = Sc, Sb, Sn, Cr or Ge) thin films grown epitaxially on MgO substrates using Time- and Frequency-Domain Thermoreflectance. They found that these high entropy oxides possess amorphous-like thermal conductivities, which drop by a factor of two to $\sim$1.4 W m^{-1} K^{-1} when a sixth cation is added, regardless of the mass added (Fig. 7a). They attributed these low thermal conductivities to local ionic charge disorder in addition to mass and strain field contrast. Another advantage of these high entropy oxides is that they possess the highest ratio of elastic modulus to thermal conductivity of any isotropic crystal (Fig. 7b), as the local ionic charge disorder effectively reduces thermal conductivity without compromising mechanical stiffness.

Junqin Li *et al.* fabricated multi-element telluride $(Sn_{0.7}Ge_{0.2}Pb_{0.1})_{1-x}Mn_{1.1x}Te$[77] and half Heusler $Nb_{1-x}(HfZrMoVTi)_xFeSb$.[16] The lattice thermal conductivities were 0.32 W m^{-1} K^{-1} at 900 K for $(Sn_{0.7}Ge_{0.2}Pb_{0.1})_{0.75}Mn_{0.275}Te$ and 2.5 W m^{-1} K^{-1} at 873 K for $Nb_{0.6}(HfZrMoVTi)_{0.4}FeSb$. Compared to SnTe or NbFeSb, the reduction in the thermal conductivities is 78% and 55%, respectively, and the value for the HEC telluride is lower than the amorphous limit of SnTe. Both HECs contain nanoscale second phase precipitates, therefore the influence of multielement on lattice thermal conductivity was not quantified.

Yan *et al.*[78] fabricated single phase $(Hf_{0.2}Zr_{0.2}Ta_{0.2}Nb_{0.2}Ti_{0.2})C$ using high-energy ball milling and spark plasma sintering. The high entropy carbides exhibited a much lower thermal

Table 1 Types of HECs and design models for certain applications

Application	HECs under investigation	Design model
Low thermal conductivity	Oxides[8]	MD + Green–Kubo formula
Thermoelectric	Chalcogenides,[6,7] half Heusler[6,16]	DFT + Boltzmann transport equations
Structural materials	Carbides,[20,33,42,57,59,60,70] Borides,[14,71,72] Nitrides[73]	DFT + hardness models
Catalyst	Oxides[47,74]	DFT
Dielectrics	Oxides[12]	DFT
Magnetic	Oxides[67,75,76]	DFT

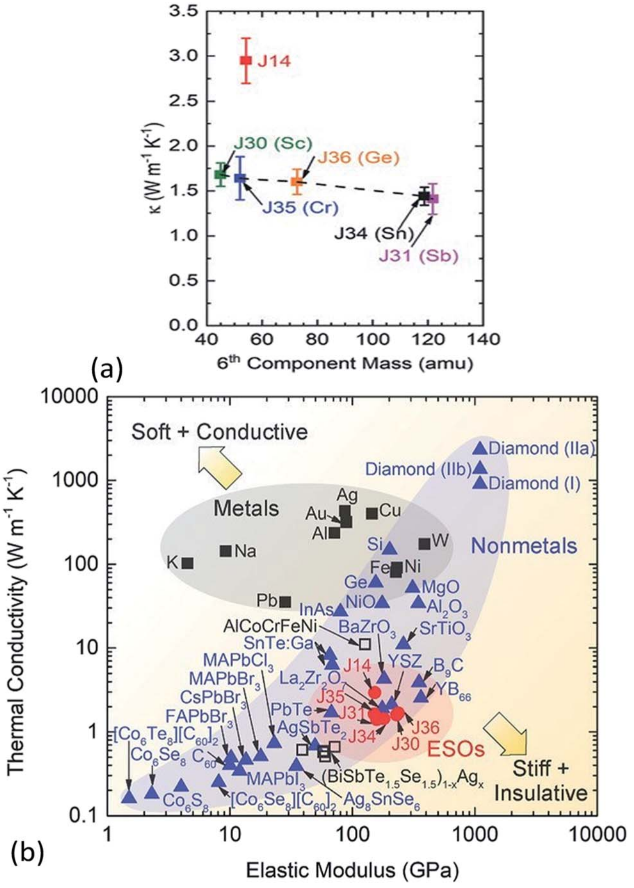

Fig. 7 (a) Thermal conductivity (κ) of six-cation MgCoNiCuZnXO$_6$ (X = Sc, Sb, Sn, Cr or Ge) high entropy oxides as a function of sixth atomic mass. The five-cation MgCoNiCuZnO$_5$ (J14 in red) is also shown at its average cation mass as a reference. (b) Thermal conductivity (κ) *versus* elastic modulus (E) for isotropic crystals at room temperature. The metals (squares) group has a subset of HEAs (open squares) and the non-metals (blue triangles) group has a subset of entropy stabilized oxides (ESOs, red circles). Reproduced with permission. Copyright 2018, John Wiley and Sons.[8]

conductivity (6.45 W m^{-1} K^{-1}) than the binary carbides HfC (29.3 W m^{-1} K^{-1}) and TaC (33.5 W m^{-1} K^{-1}) at room temperature. They attributed the thermal conductivity reduction to significant phonon scattering by the distorted anion sublattice. They proposed that the lattice distortion in (Hf$_{0.2}$Zr$_{0.2}$Ta$_{0.2}$Nb$_{0.2}$Ti$_{0.2}$)C occurs mainly through the anion sublattice, based on the fact that (Hf$_{0.2}$Zr$_{0.2}$Ta$_{0.2}$Nb$_{0.2}$Ti$_{0.2}$)C and (Mg$_{0.2}$Co$_{0.2}$Ni$_{0.2}$Cu$_{0.2}$Zn$_{0.2}$)O have similar rock-salt structures, and in (Mg$_{0.2}$Co$_{0.2}$Ni$_{0.2}$Cu$_{0.2}$Zn$_{0.2}$)O the distortion from an ideal rock-salt structure occurs primarily through disorder of the anion sublattice, which was confirmed by an extended X-ray absorption fine structure (EXAFS) analysis.[64] It is worth mentioning that the carbon stoichiometry of the samples was not analysed, which has an effect on the thermal conductivity due to phonon scattering by carbon vacancies.[79]

Gild *et al.*[18] fabricated eight single phase high entropy fluorite oxides (HEFO) with five principal cations (in addition to a four-principal-cation (Hf$_{0.25}$Zr$_{0.25}$Ce$_{0.25}$Y$_{0.25}$)O$_{2-\delta}$ as a starting point and baseline) by high energy ball milling, spark plasma sintering, and annealing in air. These single-phase high entropy oxides possess lower thermal conductivities than 8 mol% Y$_2$O$_3$-stabilized ZrO$_2$ (8YSZ), and the lowest one is 1.1 W m^{-1} K^{-1} for (Hf$_{0.25}$Zr$_{0.25}$Ce$_{0.25}$)(Y$_{0.125}$Ca$_{01.25}$)O$_{2-\delta}$, which is almost half of the value of 8YSZ (2 W m^{-1} K^{-1}). The reduced thermal conductivities are likely related to increased phonon scattering in the system due to multiple metal cations, which can lead to reductions in the phonon mean free path due to scattering from mass and bond disorder. They concluded that high-entropy effects do appear to reduce thermal conductivities in general. K. Chen *et al.*[80] prepared single phase (Ce$_{0.2}$Zr$_{0.2}$Hf$_{0.2}$Sn$_{0.2}$Ti$_{0.2}$)O$_2$ using the same methods, and obtained a room-temperature thermal conductivity of 1.28 W m^{-1} K^{-1}.

5.1.2 Modelling. The modelling of Lattice thermal conductivity for alloys and solid solutions using phenomenological equations was developed in the mid-part of the last century. In 1955, Klemens developed a phenomenological model[81] for impurity scattering based on second-order perturbation theory. Considering mass difference, local changes in the elastic constants and elastic strain, he found that phonon scattering rates by crystalline impurities have a quartic dependence on the frequency.

$$\tau_\mathrm{d}^{-1} = A\omega^4 \tag{6}$$

where τ_d is a constant relaxation time determined by point defect scattering, ω is the phonon frequency, and A is a fitting parameter and is independent of temperature. In the following years, Callaway[82] (inclusion of 3-phonon N-process) and Abeles[83] (extension to high temperatures) improved this model and applied it to various alloy systems. The Klemens–Callaway model[82] is described by

$$\kappa = \frac{k_\mathrm{B}}{2\pi v_\mathrm{s}}\left(\frac{k_\mathrm{B}T}{\hbar}\right)^3 \int_0^{T_\mathrm{D}/T} \tau \frac{x^4 \mathrm{e}^x}{(\mathrm{e}^x - 1)^2}\mathrm{d}x \tag{7}$$

where the fundamental constants k_B and $\hbar$ have their usual meaning, $x = \hbar\omega/k_\mathrm{B}T$, v_s is the speed of sound, and T_D is the Debye temperature. This model assumes a Debye spectrum of phonon frequencies with frequency-dependent relaxation times, and the point defect scattering effect is included in the expression of constant relaxation time τ. Although the model has been quite successful in fitting the experimental data of several solid solutions, it has limited fitting ability for high entropy compounds as there is only one fitting parameter for point defect scattering ('A' in eqn (6)). It also has limited predictive power due to the phenomenological nature of this model. However, it does provide some fundamental understanding of alloying on lattice thermal conductivity, which provides some useful conceptual guidance for lowering the thermal conductivity through solid solution design, such as larger mass contrast favours lower thermal conductivity.

An alternative approach to calculate lattice thermal conductivity is to use molecular dynamics,[84] including both equilibrium molecular dynamics (EMD) using the Green–Kubo formula, and non-equilibrium molecular dynamics (NEMD), which directly creates a temperature gradient in a large supercell. A. Giri *et al.*[85,86] employed the widely used 12–6 Lennard Jones (LJ) potential and NEMD method to investigate the lattice thermal conductivity of a five component solid solution. They found that the thermal conductivity reduction due to mass scattering alone reached a critical point, and a further decrease in thermal conductivity requires a change in local strain-field.[86] For example, comparing 2-component and 5-component solid solutions, only introducing mass contrast results in a one third reduction of thermal conductivity, but by changing the interatomic potential parameter (a way to introduce strain field fluctuation) plus mass contrast, the reduction can be more than a half. They also found that the thermal conductivity of solid solutions with an ordered sublattice had a pronounced temperature dependence in comparison to their fully disordered counterparts. The reason is that in ordered systems, anharmonic effects result in large temperature dependencies of thermal conductivities, while in disordered systems, impurity scattering leads to a largely reduced dependence on temperature.[85]

M. Lim *et al.*[87] used the EMD method to study the thermal conductivity of J14 ($(Mg_{0.2}Co_{0.2}Ni_{0.2}Cu_{0.2}Zn_{0.2})O$) as well as J14 plus Sc, Sn, Cr, or Ge in equal-molar cation proportions (Fig. 8). The simulations used a Buckingham potential, whose parameters were taken from MgO, plus coulombic electrostatic forces where the charge values were obtained from DFT calculations. By manipulating the mass and charges, it was shown that atomic charge disorder should be included to explain the low thermal conductivity of the experimental data of these high entropy oxides. For the MD simulations discussed above, it is worth noting that the interatomic potentials in these models are oversimplified compared with a real system due to the difficulties in developing highly reliable potentials for the complex high entropy systems. The advantage of the MD simulations is that they provide some insight at the atomic scale to explain the low thermal conductivity behaviour of HECs.

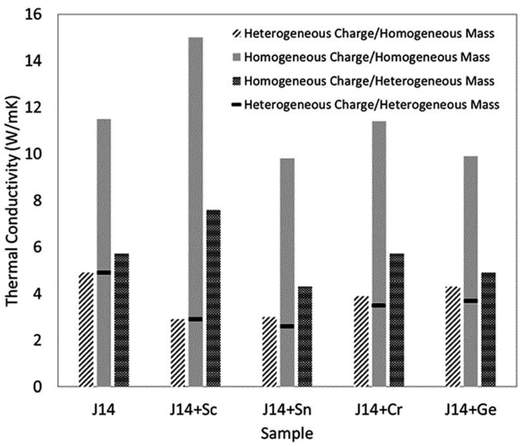

Fig. 8 Thermal conductivities using different combinations in molecular dynamics simulations, in order to show the influence of charge disorder and mass contrast on thermal conductivity. The systems are J14 ($(Mg_{0.2}Co_{0.2}Ni_{0.2}Cu_{0.2}Zn_{0.2})O$), and J14 plus Sc, Sn, Cr, or Ge in equal-molar cation proportions. Reproduced with permission. Copyright 2019, AIP Publishing.[87]

DFT provides a general framework for modelling complex atomic interactions. As a parameter free method, DFT can provided input parameters to other formalism for lattice thermal conductivity calculations. Due to its high computational cost, DFT has not yet been used for high entropy systems, while its application for binary solid solution has given some promising results. For instance, A. Henry *et al.*[88] used EMD to simulate the thermal conductivity of $In_xGa_{1-x}As$, in which the parameters for the interatomic potentials were determined using DFT data. Other approaches include calculating interatomic force constants (IFCs) using DFT, then using these IFCs with the Peierls–Boltzmann transport (PBT) equation (*e.g.* as implemented in Sheng BTE[89]) or Green's functions.[90] It is worth noting that virtual crystal approximation (VCA), which is usually used to calculate the thermal conductivity of alloys,[91] is not suitable for high entropy compounds, as charge disorder needs to be considered.[8] There is continuous effort to develop new phonon transport theory for disordered systems.[92] With the rapidly growing computation power for large scale DFT calculation, DFT based thermal conductivity modelling of HECs is emerging.

5.2 Thermoelectric properties

The electrical conductivity of high entropy sulfide $Cu_3Sn_{1+x}MgGeZnS_9$ (x = 0,0.1,0.2) shows an interesting temperature dependence[7] (Fig. 9). Below 523 K, $Cu_5Sn_{1.1}MgGeZnS_9$ first shows metallic behavior, then the electrical conductivity shows a small maximum; while $Cu_5Sn_{1.2}MgGeZnS_9$ shows semiconducting behavior. The authors attribute the behavior to the thermal activation of carriers and localized states introduced by disorder, but this suggestion needs further electronic structure studies to support it. It is worth noting that some high entropy oxides, such as $Sr(Zr_{0.2}Sn_{0.2}Ti_{0.2}Hf_{0.2}Nb_{0.2})O_3$, are not electrically conductive, although they should have dopant carriers based on the valence of their cations. The reason for this is still unclear. Again, further electronic structure studies including DFT calculations would be useful to clarify this.

The high entropy concept is also beneficial for increasing thermopower, also known as Seebeck coefficient, which is a measure of the magnitude of an induced thermoelectric voltage in response to a temperature difference across a material. The

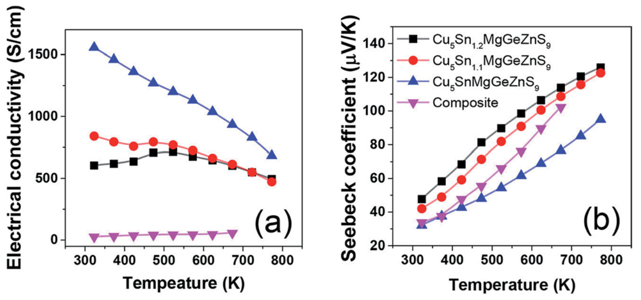

Fig. 9 Temperature dependent (a) electrical conductivity and (b) Seebeck coefficient of high entropy sulfide $Cu_5Sn_{1+x}MgGeZnS_9$ (x = 0, 0.1, 0.2). The values for Cu_3SnS_4–Cu_2MgGeS_4–ZnS composite are also shown for comparison. Reproduced under the terms of the CC-BY 4.0 license. Copyright 2018, the authors, published by ACS Publications.[7]

randomly distributed atoms increase the crystal structure symmetry and hence band symmetry, which is favorable for achieving high thermopower. Liu *et al.*[6] reported that the room temperature thermopower of (Cu/Ag)(In/Ga)Te_2- and Cu_2(S/Se/Te)-based multicomponent materials increases with configurational entropy. Recent studies also show that entropy favors a rhombohedral-to-cubic structure transition in GeSe, when $AgSbSe_2$ (ref. 93) or $AgBiSe_2$ (ref. 94) was added to increase the entropy of the system. Consequently, the thermopower is improved.

5.3 Ionic conductivity for Li-ion battery

D. Bérardan *et al.*[13] fabricated single phase $(MgCoNiCuZn)_{1-x-y}Ga_yA_xO$ (A = Li, Na, K). Firstly, they confirmed that these materials were electronic insulators by investigating the evolution of the current density during a 1 V potential step over 2 days with blocking electrodes. Then they found that the room temperature Li+ conductivity of the Li >20% (mole% on A-site) compound exceeds that of LiPON by 2 orders of magnitude (Fig. 10), which makes these HECs very attractive for applications as solid electrolytes. The ionic conduction probably occurs through the oxygen vacancies, which are created by charge compensation when a monovalent element (*e.g.* Li+) is introduced, and larger ionic conductivity values could probably be obtained by optimizing the concentration or ordering of oxygen vacancies as well as the size of the divalent cations in the compound.

However, the HEFOs fabricated by Gild *et al.*[18] showed significantly lower ionic conductivities than 8 mol% Y_2O_3-stabilized ZrO_2 (8YSZ). Arrhenius plots of $\ln(\sigma T)$ *vs.* 1000 T gave similar activation energies of 1.14–1.29 eV for all the high entropy oxides. They attributed the lower ionic conductivity to the much higher doping levels of the HEFOs compared to 8YSZ.

5.4 Mechanical properties

There have been only a few reports on the mechanical properties of HECs and these have focused on transition metal carbides. Csanádi *et al.*[42] investigated the nanoindentation of (Hf–Ta–Zr–Nb)C and found that the HEC had a higher indentation modulus than all of the monocarbides, and 8% higher than a rule of mixtures average of the values for the individual monocarbides (Fig. 11a). The indentation hardness was notably higher for the HEC (36.1 ± 1.6 GPa) compared to the hardest monocarbide HfC (31.5 ± 1.3 GPa) and the binary carbide (Hf–Ta)C (32.9 ± 1.8 GPa), and 30% higher than the value for the rule of mixtures (27.7 GPa) (Fig. 11b). Yan X *et al.*[78] reported elastic (nanoindentation) and Vicker's hardness results for (Ti,Zr,Hf,Ta,Nb,Ta)C and found that they were comparable to those of the monocarbides reported in the literature. However, the HEC had a theoretical density of only 93%, which would have resulted in a relatively low Vicker's hardness. Sarker P *et al.*[20] synthesised several five transition metal containing carbides and found a general increase in the nanoindentation elastic modulus and hardness compared to the monocarbides, comparable to that reported by Csanadi *et al.*[70] Ye *et al.*[57] have reported a very high nanoindentation hardness for (Ti,Zr,Hf,Nb,Ta)C of 40.6 GPa, and also an indentation elastic modulus higher than the rule of mixture value for the monocarbides obtained from the literature. They also found the indentation fracture behaviour and properties to be similar to those of the monocarbides reported in the literature.

Harrington T. J. *et al.*[59] investigated the relationship between the nanoindentation elastic modulus and hardness of several

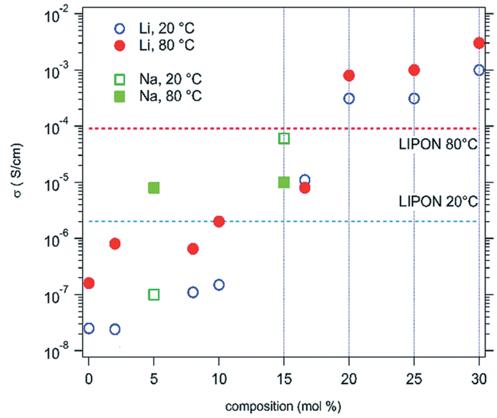

Fig. 10 Ionic conductivities for high entropy $(MgCoNiCuZn)_{1-x-y}Ga_yA_xO$ samples, where A = Li (circles) or Na (squares). The values usually observed for a LiPON solid conductor are also shown for comparison. Reproduced under the terms of the CC-BY 4.0 license. Copyright 2016, the authors, published by RSC Publishing.[13]

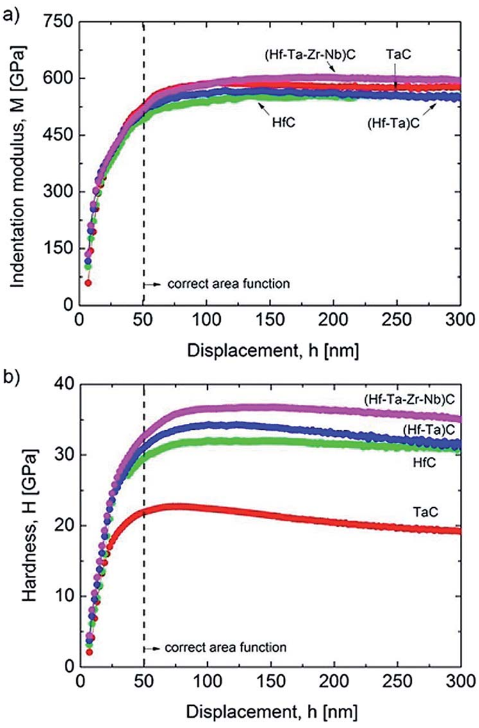

Fig. 11 Comparison of: (a) indentation modulus; and (b) hardness depth-profiles of the mono, binary and high-entropy carbide (Hf–Ta–Zr–Nb)C. The results were averaged from 64 indents made per sample, following rejection of those close to grain boundaries and pores. Reproduced under the terms of the CC-BY 4.0 license. Copyright 2018, the authors, published by Springer Nature.[42]

five transition metal carbides with their electronic properties. They found a good correlation between these properties and the Valence Electron Concentration (VEC), with the indentation elastic modulus increasing and the hardness decreasing with VEC increasing from 8.4 to 9.4. The origin of the reported increased yield stress of HECs compared to the mono and binary carbides may also be related to the local lattice distortions in a similar way to solid solution hardening in metal alloys.[95] The theories for metals are limited to small concentrations of solute atoms, and new approaches are needed to describe the effect of multi-elements on yield in HECs. In order to understand the plasticity of HECs we need to know their dislocation slip systems. The plastic deformation behaviour of group IV and V transition metal carbides is still being debated. It is generally considered that the group IV carbides slip on $\{011\}$ planes, while the group V carbides slip on $\{111\}$.[96–102] This therefore raised the interesting question of what is the dominant slip system of (Zr,Hf,Nb,Ta)C. In recent work by Csanadi *et al.*[70] they found from analysis of slip traces in micropillar compression experiments (effectively single crystal) that the dominant slip system for the monocarbides of Ta and Hf, and (Zr,Hf,Nb,Ta)C, was $\{110\}\ \langle 1\bar{1}0\rangle$ (Fig. 12b). They also found a significantly higher yield stress for the HEC compared to that of the monocarbides (58% higher compared to HfC) (Fig. 12a) while retaining a ductility comparable to TaC. The preliminary results on the mechanical properties of HEC carbides suggests that the elastic and plastic behaviour of these materials are not simply a rule of mixtures and that significant improvements in strength can be achieved.

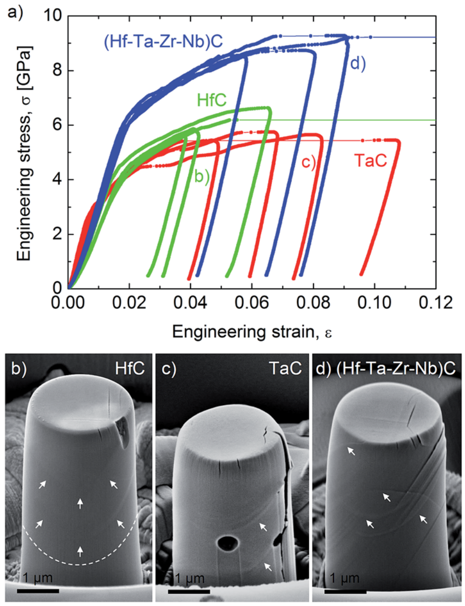

Fig. 12 (a) An enhanced yield and failure strength for the (Hf–Ta–Zr–Nb)C high entropy carbide. The stress–strain curves were obtained during micropillar compression of individual grains. Micropillars of similar orientations ($\Phi \sim 14°$) exhibit limited plasticity for grains of (b) HfC but more ductile behaviour for (c) TaC and (d) (Hf–Ta–Zr–Nb)C high-entropy carbide. Slip traces on micropillar surfaces are marked by arrows. Reproduced under the terms of the CC-BY 4.0 license. Copyright 2019, the authors, published by Springer Nature.[70]

6 Summary and outlook

The emerging topic of high entropy ceramics opens up a large new compositional space, with the possibility of new materials with enhanced properties and demonstrating new phenomena. The early work on a wide range of materials, including oxides, sulphides and carbides suggests that it is possible to synthesise single phase materials. However, closer examination of these materials may reveal some degree of ordering of the elements at the atomic scale. Some materials may turn out to be entropy stabilised to room temperature, while others may only be stable at high temperatures and show a miscibility gap on cooling. To elucidate these points will require more detailed structural analysis of these materials using a range of techniques, including direct methods such as total scattering with neutrons and X-rays, EXAFS and atom probe tomography, supported by indirect methods such as NMR and ESR.[103] It is worth noting that NMR has not yet been applied to the characterization of HECs, while it has been used for decades to study solid solutions. NMR elucidated the local atomic arrangement of Ti and Sn in $Y_2Ti_{2-x}Sn_xO_7$ pyrochlore solid solutions[104,105] supported by DFT calculations.[106]

With the development of tools to predict the synthesisability of HECs and the application of artificial intelligence, we could see the rapid emergence of interesting new materials that could open up new lines of research and applications. The modelling of these materials will be challenging because of the large number of elements involved and their mixed covalent and ionic bonding. One particularly challenging task is to find stable compounds in the multi-element composition space. To do this the Gibbs free energy of all of the possible structures needs be compared. It is not likely that brute force methods can be used in this situation because of the limits of computational power. Therefore, advanced searching algorithms need to be developed, such as the constraint satisfaction algorithm used by Abu-Odeh *et al.*[26] for the exploration of the HEA composition space.

To date, the effect of multi-elements on non-stoichiometry has not been well investigated. Considering the rich crystal chemistry of non-stoichiometric compounds and the strong dependence of their properties on deviation from stoichiometry, this presents a potentially exciting new area of research for high entropy ceramics. It raises some interesting questions: will the range of deviation from stoichiometry change; will the mechanisms of accommodating non-stoichiometry change; and will it lead to SRO; and will it change the stability of HECs?

Most of the materials studied to date have been prepared using solid state synthesis and densification by sintering. There has been some work on the synthesis of powders by chemical routes. The presence of multi-elements could lead to blockages in the synthesis of some HECs because of the formation of stable intermediate phases. The "cocktail" effect in these materials may lead to lower diffusion rates, which may present kinetic barriers to the synthesis and densification of the materials. This will require efforts to optimise the currently used processing routes or the synthesis of materials through non-equilibrium routes, for example, arc melting and rapid cooling.

With the use of increasing numbers of elements there will be greater constraints on the use of elements based on cost, toxicity and sustainability. One way in which this could be mitigated is to use inexpensive, crude, mineral precursors containing the component elements. Minerals commonly contain multi-elements and are prototypes of many functional materials. This is similar to the approach used by Xu Lu *et al.* in their work on multi-element tetrahedrite thermoelectrics.[107] This approach may also help to mitigate the potential problem of slow kinetics of reaction during synthesis by the solid state route.

The properties of functional materials are often very sensitive to composition and stoichiometry. This means that there will be a greater challenge to prepare the target composition of the precursors and also to control the volatilisation of elements during processing, particularly on an industrial scale.

In this review we have identified three fundamental questions that need to be answered and highlighted the impact of multi-elements on reducing thermal conductivity and increasing yield stress. These results could lead to the development of new thermoelectrics and ultra-high melting temperature ceramics for extreme environments. The novelty of HECs means that there are considerable opportunities to identify other interesting effects on other properties. Some interesting recent work has been reported on multi-element oxides that show promising properties as enhanced thermochemical water splitting catalysts[74] and CO oxidation catalysts.[47] There have also been a few reports of interesting magnetic effects in (Mg,Ni,Co,Zn,Cu)O based rock salt structured oxides[67,75] and perovskite structured oxides;[76] including a compressive Jahn–Teller distortion and long range magnetic order despite substantial chemical and structural disorder on the metal sublattice.

Conflicts of interest

There are no conflicts to declare.

Acknowledgements

This work was supported by Engineering and Physical Sciences Research Council (EPSRC), MASSIVE project (Grant No. EP/L017695/1). RZ acknowledges the support from Natural Science Foundation of China (11674264).

References

1 J. W. Yeh, S. K. Chen, S. J. Lin, J. Y. Gan, T. S. Chin, T. T. Shun, C. H. Tsau and S. Y. Chang, *Adv. Eng. Mater.*, 2004, **6**(5), 299–303.
2 B. Cantor, I. T. H. Chang, P. Knight and A. J. B. Vincent, *Mater. Sci. Eng., A*, 2004, **375–377**, 213–218.
3 B. S. Murty, J.-W. Yeh, S. Ranganathan and P. P. Bhattacharjee, *High-Entropy Alloys*, Elsevier, 2019.
4 M. C. Gao, J.-W. Yeh, P. K. Liaw and Y. Zhang, in *High-Entropy Alloys: Fundamentals and Applications*, Springer International Publishing, 2016.
5 C. M. Rost, E. Sachet, T. Borman, A. Moballegh, E. C. Dickey, D. Hou, J. L. Jones, S. Curtarolo and J. P. Maria, *Nat. Commun.*, 2015, **6**, 8485.
6 R. Liu, H. Chen, K. Zhao, Y. Qin, B. Jiang, T. Zhang, G. Sha, X. Shi, C. Uher, W. Zhang and L. Chen, *Adv. Mater.*, 2017, **29**(38), 1702712.
7 R.-Z. Zhang, F. Gucci, H. Zhu, K. Chen and M. J. Reece, *Inorg. Chem.*, 2018, **57**(20), 13027–13033.
8 J. L. Braun, C. M. Rost, M. Lim, A. Giri, D. H. Olson, G. N. Kotsonis, G. Stan, D. W. Brenner, J.-P. Maria and P. E. Hopkins, *Adv. Mater.*, 2018, **30**(51), 1805004.
9 V. Braic, A. Vladescu, M. Balaceanu, C. R. Luculescu and M. Braic, *Surf. Coat. Technol.*, 2012, **211**, 117–121.
10 M.-H. Hsieh, M.-H. Tsai, W.-J. Shen and J.-W. Yeh, *Surf. Coat. Technol.*, 2013, **221**, 118–123.
11 W. J. Shen, M. H. Tsai, K. Y. Tsai, C. C. Juan, C. W. Tsai, J. W. Yeh and Y. S. Chang, *J. Electrochem. Soc.*, 2013, **160**(11), C531–C535.
12 D. Bérardan, S. Franger, D. Dragoe, A. K. Meena and N. Dragoe, *Phys. Status Solidi RRL*, 2016, **10**(4), 328–333.
13 D. Bérardan, S. Franger, A. K. Meena and N. Dragoe, *J. Mater. Chem. A*, 2016, **4**(24), 9536–9541.
14 J. Gild, Y. Zhang, T. Harrington, S. Jiang, T. Hu, M. C. Quinn, W. M. Mellor, N. Zhou, K. Vecchio and J. Luo, *Sci. Rep.*, 2016, **6**, 37946.
15 J. Gild, J. Braun, K. Kaufmann, E. Marin, T. Harrington, P. Hopkins, K. Vecchio and J. Luo, *Journal of Materiomics*, 2019, DOI: 10.1016/j.jmat.2019.03.002.
16 J. Yan, F. Liu, G. Ma, B. Gong, J. Zhu, X. Wang, W. Ao, C. Zhang, Y. Li and J. Li, *Scr. Mater.*, 2018, **157**, 129–134.
17 S. Jiang, T. Hu, J. Gild, N. Zhou, J. Nie, M. Qin, T. Harrington, K. Vecchio and J. Luo, *Scr. Mater.*, 2018, **142**, 116–120.
18 J. Gild, M. Samiee, J. L. Braun, T. Harrington, H. Vega, P. E. Hopkins, K. Vecchio and J. Luo, *J. Eur. Ceram. Soc.*, 2018, **38**(10), 3578–3584.
19 W. Hume-Rothery, W. Mabbott Gilbert, K. M. Channel Evans and H. Carpenter Henry Cort, *Philos. Trans. R. Soc., A*, 1934, **233**(721–730), 1–97.
20 P. Sarker, T. Harrington, C. Toher, C. Oses, M. Samiee, J.-P. Maria, D. W. Brenner, K. S. Vecchio and S. Curtarolo, *Nat. Commun.*, 2018, **9**(1), 4980.
21 R. Ramprasad, R. Batra, G. Pilania, A. Mannodi-Kanakkithodi and C. Kim, *npj Comput. Mater.*, 2017, **3**(1), 54.
22 L. M. Ghiringhelli, J. Vybiral, S. V. Levchenko, C. Draxl and M. Scheffler, *Phys. Rev. Lett.*, 2015, **114**(10), 105503.
23 R. D. Shannon, *Acta Crystallogr., Sect. A: Cryst. Phys., Diffr., Theor. Gen. Crystallogr.*, 1976, **32**, 751.
24 I. D. Brown, *Struct. Bonding*, 2013, **158**, 11–58.
25 A. Zunger, *Phys. Rev. B: Condens. Matter Mater. Phys.*, 1980, **22**(12), 5839–5872.
26 A. Abu-Odeh, E. Galvan, T. Kirk, H. Mao, Q. Chen, P. Mason, R. Malak and R. Arróyave, *Acta Mater.*, 2018, **152**, 41–57.

27 M. C. Gao, C. Zhang, P. Gao, F. Zhang, L. Z. Ouyang, M. Widom and J. A. Hawk, *Curr. Opin. Solid State Mater. Sci.*, 2017, **21**(5), 238–251.

28 M. Widom, *J. Mater. Res.*, 2018, **33**(19), 1–18.

29 A. Sarkar, Q. Wang, A. Schiele, M. R. Chellali, S. S. Bhattacharya, D. Wang, T. Brezesinski, H. Hahn, L. Velasco and B. Breitung, *Adv. Mater.*, 2019, 1806236.

30 A. Zunger, S. Wei, L. G. Ferreira and J. E. Bernard, *Phys. Rev. Lett.*, 1990, **65**(3), 353–356.

31 H. Zhang, D. Hedman, P. Feng, G. Han and F. Akhtar, *Dalton Trans.*, 2019, **48**, 5161–5167.

32 A. van de Walle, *Calphad*, 2009, **33**(2), 266–278.

33 B. Ye, T. Wen, M. C. Nguyen, L. Hao, C.-Z. Wang and Y. Chu, *Acta Mater.*, 2019, **170**, 15–23.

34 P. Soven, *Phys. Rev.*, 1967, **156**(3), 809–813.

35 N. Saunders and A. P. Miodownik, *CALPHAD (Calculation of Phase Diagrams): A Comprehensive Guide*, Pergamon, 1998.

36 S. Gorsse and N. O. Senkov, *Entropy*, 2018, **20**(12), 899.

37 R. K. Pathria and P. D. Beale, *Statistical Mechanics*, Elsevier, 2011.

38 J. M. Sanchez, *Phys. Rev. B: Condens. Matter Mater. Phys.*, 2010, **81**(22), 224202.

39 J. M. Sanchez, *Phys. Rev. B: Condens. Matter Mater. Phys.*, 1993, **48**(18), 14013–14015.

40 D. Lerch, O. Wieckhorst, G. L. W. Hart, R. W. Forcade and S. Müller, *Modell. Simul. Mater. Sci. Eng.*, 2009, **17**(5), 055003.

41 Y. Lederer, C. Toher, K. S. Vecchio and S. Curtarolo, *Acta Mater.*, 2018, **159**, 364–383.

42 E. Castle, T. Csanádi, S. Grasso, J. Dusza and M. Reece, *Sci. Rep.*, 2018, **8**(1), 8609.

43 W. Hong, F. Chen, Q. Shen, Y.-H. Han, W. G. Fahrenholtz and L. Zhang, *J. Am. Ceram. Soc.*, 2019, **102**(4), 2228–2237.

44 A. Sarkar, R. Djenadic, N. J. Usharani, K. P. Sanghvi, V. S. K. Chakravadhanula, A. S. Gandhi, H. Hahn and S. S. Bhattacharya, *J. Eur. Ceram. Soc.*, 2017, **37**(2), 747–754.

45 M. Biesuz, L. Spiridigliozzi, G. Dell'Agli, M. Bortolotti and V. M. Sglavo, *J. Mater. Sci.*, 2018, **53**(11), 8074–8085.

46 A. Sarkar, L. Velasco, D. Wang, Q. Wang, G. Talasila, L. de Biasi, C. Kübel, T. Brezesinski, S. S. Bhattacharya, H. Hahn and B. Breitung, *Nat. Commun.*, 2018, **9**(1), 3400.

47 H. Chen, J. Fu, P. Zhang, H. Peng, C. W. Abney, K. Jie, X. Liu, M. Chi and S. Dai, *J. Mater. Chem. A*, 2018, **6**(24), 11129–11133.

48 Q. Wang, A. Sarkar, D. Wang, L. Velasco, R. Azmi, S. S. Bhattacharya, T. Bergfeldt, A. Düvel, P. Heitjans, T. Brezesinski, H. Hahn and B. Breitung, *Energy Environ. Sci.*, 2019, DOI: 10.1039/C9EE00368A.

49 A. Sarkar, C. Loho, L. Velasco, T. Thomas, S. S. Bhattacharya, H. Hahn and R. Djenadic, *Dalton Trans.*, 2017, **46**(36), 12167–12176.

50 Z. Lei, X. Liu, R. Li, H. Wang, Y. Wu and Z. Lu, *Scr. Mater.*, 2018, **146**, 340–343.

51 Y. Sharma, B. L. Musico, X. Gao, C. Hua, A. F. May, A. Herklotz, A. Rastogi, D. Mandrus, J. Yan, H. N. Lee, M. F. Chisholm, V. Keppens and T. Z. Ward, *Phys. Rev. Mater.*, 2018, **2**(6), 060404.

52 P. B. Meisenheimer, T. J. Kratofil and J. T. Heron, *Sci. Rep.*, 2017, **7**(1), 13344.

53 L. E. Cross, *Ferroelectrics*, 1987, **76**(1), 241–267.

54 C. J. Vineis, A. Shakouri, A. Majumdar and M. G. Kanatzidis, *Adv. Mater.*, 2010, **36**, 3970–3980.

55 D. B. Miracle and O. N. Senkov, *Acta Mater.*, 2017, **122**, 448–511.

56 E. J. Pickering and N. G. Jones, *Int. Mater. Rev.*, 2016, **61**(3), 183–202.

57 B. Ye, T. Wen, K. Huang, C. Z. Wang and Y. Chu, *J. Am. Ceram. Soc.*, 2019, **102**(7), 4344–4352.

58 J. Zhou, J. Zhang, F. Zhang, B. Niu, L. Lei and W. Wang, *Ceram. Int.*, 2018, **44**(17), 22014–22018.

59 T. J. Harrington, J. Gild, P. Sarker, C. Toher, C. M. Rost, O. F. Dippo, C. McElfresh, K. Kaufmann, E. Marin, L. Borowski, P. E. Hopkins, J. Luo, S. Curtarolo, D. W. Brenner and K. S. Vecchio, *Acta Mater.*, 2019, **166**, 271–280.

60 J. Dusza, P. Švec, V. Girman, R. Sedlák, E. G. Castle, T. Csanádi, A. Kovalčíková and M. J. Reece, *J. Eur. Ceram. Soc.*, 2018, **38**(12), 4303–4307.

61 C. Peng, X. Gao, M. Wang, L. Wu, H. Tang, X. Li, Q. Zhang, Y. Ren, F. Zhang, Y. Wang, B. Zhang, B. Gao, Q. Zou, Y. Zhao, Q. Yang, D. Tian, H. Xiao, H. Gou, W. Yang, X. Bai, W. L. Mao and H.-k. Mao, *Appl. Phys. Lett.*, 2019, **114**(1), 011905.

62 T. F. Kelly and D. J. Larson, *Annu. Rev. Mater. Res.*, 2012, **42**(1), 1–31.

63 M. R. Chellali, A. Sarkar, S. H. Nandam, S. S. Bhattacharya, B. Breitung, H. Hahn and L. Velasco, *Scr. Mater.*, 2019, **166**, 58–63.

64 C. M. Rost, Z. Rak, D. W. Brenner and J.-P. Maria, *J. Am. Ceram. Soc.*, 2017, **100**(6), 2732–2738.

65 D. A. Keen and A. L. Goodwin, *Nature*, 2015, **521**, 303.

66 D. Berardan, A. K. Meena, S. Franger, C. Herrero and N. Dragoe, *J. Alloys Compd.*, 2017, **704**, 693–700.

67 Z. Rák, J. P. Maria and D. W. Brenner, *Mater. Lett.*, 2018, **217**, 300–303.

68 G. Anand, A. P. Wynn, C. M. Handley and C. L. Freeman, *Acta Mater.*, 2018, **146**, 119–125.

69 Z. Rak, C. M. Rost, M. Lim, P. Sarker, C. Toher, S. Curtarolo, J. P. Maria and D. W. Brenner, *J. Appl. Phys.*, 2016, **120**(9), 095105.

70 T. Csanadi, E. Castle, M. J. Reece and J. Dusza, *Sci. Rep.*, 2019, **9**(1), 10200.

71 G. Tallarita, R. Licheri, S. Garroni, R. Orrù and G. Cao, *Scr. Mater.*, 2019, **158**, 100–104.

72 P. H. Mayrhofer, A. Kirnbauer, P. Ertelthaler and C. M. Koller, *Scr. Mater.*, 2018, **149**, 93–97.

73 Q.-W. Xing, S.-Q. Xia, X.-H. Yan and Y. Zhang, *J. Mater. Res.*, 2018, **33**(19), 3347–3354.

74 S. Zhai, J. Rojas, N. Ahlborg, K. Lim, M. F. Toney, H. Jin, W. C. Chueh and A. Majumdar, *Energy Environ. Sci.*, 2018, **11**(8), 2172–2178.

75 M. P. Jimenez-Segura, T. Takayama, D. Bérardan, A. Hoser, M. Reehuis, H. Takagi and N. Dragoe, *Appl. Phys. Lett.*, 2019, **114**(12), 122401.

76 R. Witte, A. Sarkar, R. Kruk, B. Eggert, R. A. Brand, H. Wende and H. Hahn, *Phys. Rev. Mater.*, 2019, **3**(3), 034406.

77 L. Hu, Y. Zhang, H. Wu, J. Li, Y. Li, M. McKenna, J. He, F. Liu, S. J. Pennycook and X. Zeng, *Adv. Energy Mater.*, 2018, **8**(29), 1802116.

78 X. Yan, L. Constantin, Y. Lu, J.-F. Silvain, M. Nastasi and B. Cui, *J. Am. Ceram. Soc.*, 2018, **101**(10), 4486–4491.

79 M. M. Opeka, I. G. Talmy, E. J. Wuchina, J. A. Zaykoski and S. J. Causey, *J. Eur. Ceram. Soc.*, 1999, **19**(13), 2405–2414.

80 K. Chen, X. Pei, L. Tang, H. Cheng, Z. Li, C. Li, X. Zhang and L. An, *J. Eur. Ceram. Soc.*, 2018, **38**(11), 4161–4164.

81 P. G. Klemens, *Proc. Phys. Soc., London, Sect. A*, 1955, **68**(12), 1113.

82 J. Callaway and H. C. von Baeyer, *Phys. Rev.*, 1960, **120**(4), 1149.

83 B. Abeles, *Phys. Rev.*, 1963, **131**(5), 1906–1911.

84 P. Chantrenne, in *Microscale and Nanoscale Heat Transfer*, 2007, vol. 107, pp. 155–180.

85 A. Giri, J. L. Braun and P. E. Hopkins, *J. Appl. Phys.*, 2018, **123**(1), 015106.

86 A. Giri, J. L. Braun, C. M. Rost and P. E. Hopkins, *Scr. Mater.*, 2017, **138**, 134–138.

87 M. Lim, Z. Rak, J. L. Braun, C. M. Rost, G. N. Kotsonis, P. E. Hopkins, J. P. Maria and D. W. Brenner, *J. Appl. Phys.*, 2019, **125**(5), 055105.

88 H. R. Seyf, L. Yates, T. L. Bougher, S. Graham, B. A. Cola, T. Detchprohm, M.-H. Ji, J. Kim, R. Dupuis, W. Lv and A. Henry, *npj Comput. Mater.*, 2017, **3**(1), 49.

89 W. Li, J. Carrete, N. A. Katcho and N. Mingo, *Comput. Phys. Commun.*, 2014, **185**(6), 1747–1758.

90 M. Arrigoni, J. Carrete, N. Mingo and G. K. H. Madsen, *Phys. Rev. B*, 2018, **98**(11), 115205.

91 L. Lindsay, C. Hua, X. L. Ruan and S. Lee, *Materials Today Physics*, 2018, **7**, 106–120.

92 F. DeAngelis, M. G. Muraleedharan, J. Moon, H. R. Seyf, A. J. Minnich, A. J. H. McGaughey and A. Henry, *Nanoscale Microscale Thermophys. Eng.*, 2018, **23**(2), 81–116.

93 Z. Huang, S. A. Miller, B. Ge, M. Yan, S. Anand, T. Wu, P. Nan, Y. Zhu, W. Zhuang, G. J. Snyder, P. Jiang and X. Bao, *Angew. Chem., Int. Ed.*, 2017, **56**(45), 14113–14118.

94 S. Roychowdhury, T. Ghosh, R. Arora, U. V. Waghmare and K. Biswas, *Angew. Chem.*, 2018, **130**(46), 15387–15391.

95 O. N. Senkov, J. M. Scott, S. V. Senkova, D. B. Miracle and C. F. Woodward, *J. Alloys Compd.*, 2011, **509**(20), 6043–6048.

96 N. De Leon, X.-x. Yu, H. Yu, C. R. Weinberger and G. B. Thompson, *Phys. Rev. Lett.*, 2015, **114**(16), 165502.

97 S. Kiani, J.-M. Yang and S. Kodambaka, *J. Am. Ceram. Soc.*, 2015, **98**(8), 2313–2323.

98 F. R. Chien, X. J. Ning and A. H. Heuer, *Acta Mater.*, 1996, **44**(6), 2265–2283.

99 Y. Kumashiro, Y. Nagai, H. Katō, E. Sakuma, K. Watanabe and S. Misawa, *J. Mater. Sci.*, 1981, **16**(10), 2930–2933.

100 Y. Kumashiro, A. Itoh, T. Kinoshita and M. Sobajima, *J. Mater. Sci.*, 1977, **12**(3), 595–601.

101 D. J. Rowcliffe and G. E. Hollox, *J. Mater. Sci.*, 1971, **6**(10), 1261–1269.

102 D. W. Lee and J. S. Haggerty, *J. Am. Ceram. Soc.*, 1969, **52**(12), 641–647.

103 S. J. L. Billinge and I. Levin, *Science*, 2007, **316**(5824), 561.

104 M. R. Mitchell, S. W. Reader, K. E. Johnston, C. J. Pickard, K. R. Whittle and S. E. Ashbrook, *Phys. Chem. Chem. Phys.*, 2011, **13**(2), 488–497.

105 S. W. Reader, M. R. Mitchell, K. E. Johnston, C. J. Pickard, K. R. Whittle and S. E. Ashbrook, *J. Phys. Chem. C*, 2009, **113**(43), 18874–18883.

106 S. E. Ashbrook and D. McKay, *Chem. Commun.*, 2016, **52**(45), 7186–7204.

107 X. Lu and D. T. Morelli, *Phys. Chem. Chem. Phys.*, 2013, **15**(16), 5762–5766.